Applied Catalysis B: Environmental 148–149 (2014) 377–386

Contents lists available at ScienceDirect

Applied Catalysis B: Environmental

journal homepage: www.elsevier.com/locate/apcatb

Adsorption–desorption behavior and mechanism of dimethyl disulfide in liquid hydrocarbon streams on modified Y zeolites

Dezhi Yi, Huan Huang, Xuan Meng, Li Shi*

The State Key Laboratory of Chemical Engineering, East China University of Science and Technology, Shanghai 200237, People's Republic of China

ARTICLE INFO

Article history:
Received 6 August 2013
Received in revised form 31 October 2013
Accepted 15 November 2013
Available online 22 November 2013

Keywords:
Desulfurization
Dimethyl sulfide
Zeolite
Acidic sites
Activation energy

ABSTRACT

Removal of organic sulfur compounds from its solution has been investigated by using adsorption on the ion-exchanged Y zeolites. Effects of metal cations, calcination temperature and reaction temperature on the removal efficiency have been accessed by performing the dynamic and static tests. The adsorbents were characterized by X-ray fluorescence analysis (XRF), X-ray diffraction (XRD), thermal analysis (TGA) and X-ray photoelectron spectroscopy (XPS). Pyridine-FTIR spectroscopy showed that Lewis acid is contributed to increase the adsorption capacity, while Brønsted acid has an adverse effect on the desulfurization capability. Spectral shifts of the ν(C–S), ν(S–S) and ν(Cu–S) vibrations of the Cu–Y zeolite after adsorption of DMDS were measured with the Raman spectrum. In situ Fourier transform infrared (FTIR) and temperature-programmed desorption of DMDS (DMDS–TPD) results indicated that the adsorption mechanisms on Cu(I)-Y zeolite was the S–M (σ) bond which formed to increase adsorption bond energy of DMDS.

1. Introduction

Dimethyl disulfide (DMDS), with a very low odor threshold concentrations as low as 0.1 ppb [1], is a volatile organic compound containing sulfur. DMDS may cause toxic effects if inhaled or absorbed through skin. DMDS is known to be produced in aerobic or anaerobic environments, mainly from natural sources, hydrocarbon mixtures at petroleum refining processes, the wood-pulping industry, sewage treatment, and energy-related activities. Because the crude oil is getting much worse and heavier in recent years, the content of DMDS exist in the liquid hydrocarbon streams especially in low hydrocarbons is getting much higher[2]. Methyl tertiary butyl ether (MTBE), which is added to gasoline to boost the octane number of gasoline, has become higher content in sulfur. As shown in Table 1, the MTBE contains various kinds of sulfur compounds including mercaptane, DMDS and so forth. Since these sulfur compounds reduce the purity of the petrochemical products, and deteriorate the process performance, they should be removed in a pretreatment process [3].

In 2009, the European Union has issued regulations that required refineries to drastically reduce the sulfur content of gasoline to less than 10 ppmw [4], and similar regulations were implemented in Beijing in 2012 [5]. In conventional removal of sulfur compounds, hydrodesulfurization (HDS) processes are carried out, using Co–Mo/Al_2O_3 or Ni–Mo/Al_2O_3 catalysts at high temperatures (300–340 °C) and pressures (20–100 atm of H_2) conditions [6]. However, HDS processes cannot meet the current sulfur level requirements, and the hydrogenation of olefins should be simultaneously minimized, because it reduces the octane number.

Contrary to the above methods, the adsorptive desulfurization has the advantages that it does not require hydrogen addition and can be operated at room temperature and atmospheric pressure. There is an ongoing effort to develop new adsorbents to remove the sulfur compounds from commercial fuels via π-complexation [7–11], van der Waals' and electrostatic interactions [12,13] and reactive adsorption by chemisorption at elevated temperatures [14,15]. Deep desulfurization on various adsorbents such as activated carbons (ACs) [16–18], modified composite oxide [19,20], and zeolite [21], has already been studied. Mikhail et al. [13] used several inexpensive solid materials (acid-activated kaolinite, acid-activated bentonite, charcoal, petroleum coke and cement kiln dust) to remove DMDS from its solution and confirmed that the acid-activated bentonite was the most suitable adsorbent at the reaction temperature of 30 °C. Jieun Lee et al. [2] used ion-exchanged zeolites to remove DMDS from C_4 hydrocarbon mixture and reported that ion exchanged zeolites were favorable adsorbents with high capacity for adsorptive removal of DMDS from gas hydrocarbon mixture at ambient conditions. For the removal of DMDS from liquid hydrocarbon streams, however, seldom investigation was found in the open literatures.

In the present study, modified Y zeolites were used as adsorbents for the removal of DMDS from liquid hydrocarbon streams.

* Corresponding author. Tel.: +21 64252274; fax: +21 64252274.
E-mail address: yyshi@ecust.edu.cn (L. Shi).

0926-3373/$ – see front matter © 2013 Elsevier B.V. All rights reserved.
http://dx.doi.org/10.1016/j.apcatb.2013.11.027

Table 1
Sulfur content analysis in MTBE.

sulfur compound	Concentration (ppm)
Methyl mercaptan	1.01
Ethyl mercaptan	<10
Butyl mercaptan	41.23
Thiophene	0.76
DMDS	45.77
Diethyl disulfide	6.68

In order to improve the desulfurization capacity, several transition metals were introduced to modify the NaY zeolite. Adsorption characteristics of DMDS on sorbents were studied by using a dynamic adsorption method in a fixed bed. The sorbents were characterized by X-ray fluorescence analysis (XRF), X-ray diffraction (XRD), thermal analysis (TGA), X-ray photoelectron spectroscopy (XPS) and pyridine-FTIR spectroscopy. The adsorbent after adsorption of DMDS was characterized by the Raman spectrum and the adsorption mechanism was also discussed on the basis of the analysis of in situ FTIR spectroscopy. Activated energy of desorption of DMDS on adsorbents was determined by the temperature programmed desorption of DMDS (DMDS–TPD).

2. Experimental

2.1. Sorbent preparation.

The starting adsorbent materials Na–Y zeolite (Si/Al = 3.26, Nankai University catalyst Co., Ltd.), was used as received and in powder form. The adsorbent were prepared by liquid-phase ion exchange (LPIE) of Na–Y with Cu^{2+}, Ni^{2+}, Co^{2+} and Ce^{3+} using a 5-fold excess of 0.5 M aqueous solution of respective metal nitrates at 90 °C for 24 h. After ion exchange, the zeolite suspension was filtered, washed thoroughly using deionized water, dried at 120 °C overnight, and then calcined at 450 °C in a muffle furnace in dry O_2 atmosphere.

Cu(I)–Y zeolite was prepared by ion-exchanging Na–Y zeolite with a $Cu(NO_3)_2$ aqueous solution (0.5 M) for 24 h followed by reduction of Cu^{2+} to Cu^{+}. The adsorbent was washed and filtered to be dried in a 120 °C oven overnight. Activation was performed at 450 °C for 5 h in pure helium to promote autoreduction of Cu^{2+} species to Cu^{+}. The autoreduction of cupric ions to cuprous ions in synthetic zeolites has been reported by several groups [22,23].

2.2. Reagents and feedstocks.

The metal nitrates were purchased from Sinopharm Chemical Reagent Co., Ltd. DMDS has been used as a model compound to measure the extent of activity of the sorbents towards sulfur compounds adsorption. To obtain the model oil for desulfurization, DMDS was placed into *n*-octane, and in the final solution, the sulfur concentration was 2000 ppm. DMDS was purchased from Aldrich and *n*-octane was purchased from Sinopharm Chemical Reagent Co., Ltd.

2.3. Sulfur adsorption experiments.

2.3.1. Dynamic tests

Dynamic tests were carried out to evaluate the capacity of the sorbents for sulfur removal. First, adsorbent samples were packed into a quartz column (length: 500 mm; internal diameter: 9 mm; bed volume: 1.25 cm^3). Then the sorbent was loaded in the middle of the reactor and the spare spaces were filled with quartz sand (20–40 mesh). The experiments were carried out under the following conditions: atmospheric pressure, LHSV (liquid hourly space velocity) 10.0 h^{-1}. The outflow oil were analyzed, quantitatively using a Agilent 6890A Gas Chromatograph and qualitatively using a Finnigan SSQ710 GC-MS. The distributions of sulfur compounds in the products were analyzed in the Agilent 6890A Gas Chromatograph coupled with a flame photometric detector (FPD). The adsorbed amount of sulfur was calculated directly from breakthrough curves.

$$\text{Desulfurizationration}\,(\%) = \left[\frac{(C_0 - C)}{C_0}\right] \times 100 \quad (1)$$

where C_0 is the initial number of moles of sulfur (mol L^{-1}), C is the final number of moles of sulfur (mol L^{-1}).

2.3.2. Static tests

Static tests were carried out at ambient temperature to evaluate the capacity of the sorbents for sulfur removal. Adsorbent (0.1 g) was added to a 15 mL sample of hydrocarbon containing sulfur in an airtight container with a shaker apparatus operating at ambient temperature for 12 h. Then the concentration of sulfur was analyzed by gas chromatography.

2.4. Characterization of adsorbents

2.4.1. X-ray diffraction

X-ray diffraction (XRD) technique was used to characterize the crystal structure. In this work, XRD patterns were obtained with a Siemens Model D-500 X-ray diffractometer equipped with Ni-filtered Cu KR radiation (40 kV, 100 mA). The 2θ scanning angle range was 5–75° with a step of 0.02° s^{-1}.

2.4.2. X-ray fluorescence analysis

The chemical composition was determined by X-ray fluorescence spectrometry (XRF-1800, Shimadzu Corporation, Japan). The quantitatively results of samples were used to analyze elements contents and their percentages

2.4.3. Acidity characterization

The amount of acid, acid density, and acid variety were measured via Fourier transform infrared (FT–IR) spectroscopy (Nicolet Company, Model Magna-IR550), using pyridine as the probe molecule. There are two varieties of acid: one is a Brønsted acid (denoted as B), whose characteristic absorption peak is observed at 1540 cm^{-1}; and the other is a Lewis acid (denoted as L), whose characteristic absorption peak is located at 1450 cm^{-1}. The pyridine adsorption, which is measured after desorption at 200 °C, is the total acid sites (T). The pyridine adsorption, which is measured after desorption at 450 °C, represents the strong acid sites (S). The difference represents the weak acid sites (W). The quantification method for Lewis acidic site and Brønsted acidic site was based on Lambert–Beer law: $A = \xi Cd$, where A is absorbance, C is sample concentration, ξ is extinction coefficient and d is sample thickness. The surface acid contents of adsorbents for Lewis acid and Brønsted acid were calculated by using empirical formulas which are obtained from the relevant experiments.

$$C_L\left(\text{mol g}^{-1}\right) = 3.73 \times 10^{-4}\ A_L \quad (2)$$

$$C_B\left(\text{mol g}^{-1}\right) = 9.90 \times 10^{-4}\ A_B \quad (3)$$

where C_L and C_B are respectively Lewis acid contents and Brønsted acid contents (mol g^{-1}), A_L and A_B are respectively peak areas in 1450 cm^{-1} (denoted as L) and in 1540 cm^{-1} (denoted as B).

2.4.4. Thermal analysis

Thermo-gravimetric (TG) curves were obtained using a TA Instruments thermal analyzer. The samples were exposed to an

increase in temperature of 10 °C min^{-1} up to 700 °C while the nitrogen flow rate was held constant at 100 mL min^{-1}.

2.4.5. Raman spectra

The Raman spectra studies were conducted on a Renishaw System 100 Raman spectrometer using 514 nm red excitation from an Ar laser. The laser power was 3 mW at the sample position. The Raman scattered light was detected perpendicular to the laser beam with a Peltier-cooled CCD detector, and the spectral resolution in all measurements was 1 cm^{-1}.

2.4.6. Temperature programmed desorption of DMDS (DMDS–TPD)

DMDS–TPD were conducted on Auto Chem 2910 (Micromeritics, USA). Approximately 100 mg of adsorbent was taken in a quartz tube and pretreated at 450 °C in helium flow for 60 min. When the temperature was lowered to 30 °C, the DMDS was injected in pulse to the sample until saturation. After that, DMDS–TPD was carried out from 30 to 500 °C at different heating rates of 5–12 °C min^{-1}. Component and composition of the effluent was analyzed by the TCD.

2.4.7. X-ray photoelectron spectroscopy

To identify the chemical state of copper ion on the adsorbent surface, XPS spectra of the samples were obtained by using a Perkin–Elmer PHI 5000 C ESCA system equipped with Mg anode. Their binding energies were corrected by the *C* 1s line at 284.6 eV. The full widths of the peak at the half maximum (FWHM) were allowed to adjust for attaining the best fitting.

2.4.8. In situ FTIR measurements

Fourier transform infrared (FTIR) spectra were collected (Magna-IR550, Nicolet Company) with a combined reactor-spectrometer system using a low-volume in situ cell with water-cooled KBr windows. For all experiments, 16.5–16.9 mg of finely ground Na–Y zeolite or Cu–Y zeolite was pressed into self-supporting wafers with a diameter of 10 mm. The wafers loaded into the cell was pretreated at 380 °C in vacuum conditions for 2 h and then cooled down to room temperature for DMDS adsorption. After adsorption, the sample was purged by vacuum for 0.5 h and subjected to the thermal desorption of the adsorbed sulfur compound in vacuum at different temperatures (50, 100, 150, 200, 250 and 300 °C) monitored by FTIR spectroscopy.

3. Results and discussion

3.1. Chemical element analysis of the adsorbents.

Chemical analysis was carried to evaluate total silicon, aluminum and metal ions by X-ray fluorescence and the results of chemical element analysis of Na–Y, Cu(II)–Y, Ni–Y, Co–Y and Ce–Y zeolites are presented in Table 2. It has been reported that metal cations which exist in the zeolite were in the form of a skeleton balance-charge after the ion-exchange process [24]. Therefore, the $n(\mathrm{mM}^{m+}+\mathrm{Na}^{+})/n(\mathrm{Al})$ ratio should be a constant value (≈1.0) and the element analysis of XRF could certify that $n(2\mathrm{Cu}^{2+}+\mathrm{Na}^{+})/n(\mathrm{Al})$, $n(2\mathrm{Ni}^{2+}+\mathrm{Na}^{+})/n(\mathrm{Al})$, $n(3\mathrm{Co}^{3+}+\mathrm{Na}^{+})/n(\mathrm{Al})$ and $n(3\mathrm{Ce}^{3+}+\mathrm{Na}^{+})/n(\mathrm{Al})$ were equal to about 1. As shown in Table 2, the $n(\mathrm{Si})/n(\mathrm{Al})$ ratio increased after the ion-exchange. It indicates that ion-exchange process caused collapse of the molecular sieve structure and dealumination of the framework.

X-ray diffraction analysis in Fig. 1 was carried out to identify the mineralogical structure of the ion-exchanged and Na–Y zeolites. No significant distinction can be observed among the XRD patterns of Cu(I)–Y, Ni–Y, Co–Y, Cu(II)–Y, Ce–Y and Na–Y. The several sharp

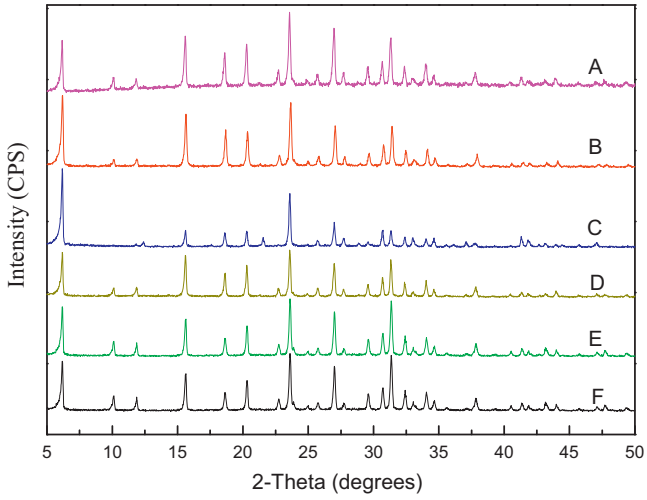

Fig. 1. X-ray diffraction patterns of the adsorbents calcinated at 450 °C: (A) Cu(I)–Y (B) Ni–Y, (C) Ce–Y, (D) Co–Y, (E) Cu(II)–Y, and (F) Na–Y.

diffraction peaks were owing to the feature of Na–Y zeolite, which showed main characteristic reflections at $2\theta = 15.64°$ and 23.64°. Only Na–Y zeolites were detected at the samples. This suggested that metal cations compensated to the skeleton structure exist as amorphous materials. Fig. 1 confirmed that the crystallinities of the adsorbents slightly decreased, compared to Na–Y zeolite, because of the framework defects caused by the introduction of metal ions.

3.2. Desulfurization performances of the modified Y zeolites.

Dynamic tests were carried out at room temperature to evaluate the desulfurization performances of the sorbents. A correlation between desulfuration and different ion-exchanged zeolites has been tested. Dynamic test results presented in Fig. 2 denoting the breakthrough curves for DMDS on the virgin Na–Y and modified Y zeolites. It can be seen from the curves that Cu(I)–Y, Co–Y and Ni–Y zeolites could absorb more sulfur than the raw Na–Y zeolite. And Cu(I)–Y zeolite showed the most excellent DMDS removal performance, which could maintain completely elimination of DMDS for 6 h. However, the desulfurization performance of Cu(II)–Y zeolite was at a low level, indicating that Cu^{+} is a key cation that interacts directly with the DMDS. On the contrary, the Ce–Y zeolite showed

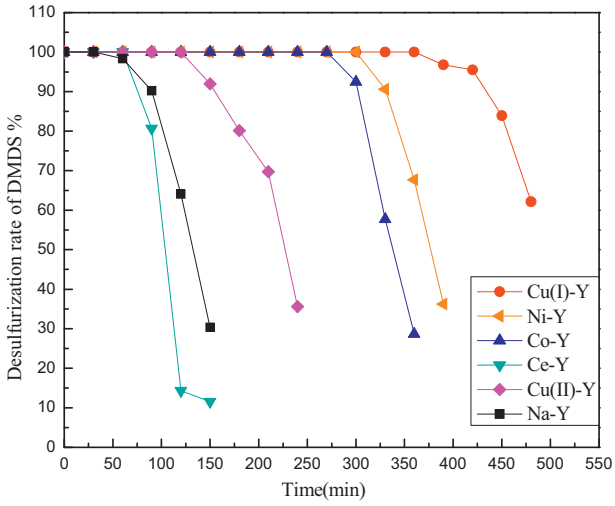

Fig. 2. Breakthrough curves for DMDS adsorption on different ion-exchanged zeolites at calcination temperature of 450 °C.

Table 2
Elemental composition of different ion-exchanged and Na–Y zeolites.

Zeolite	n(Na)/n(Al)	n(Cu)/n(Al)	n(Ni)/n(Al)	n(Co)/n(Al)	n(Ce)/n(Al)	n(Si)/n(Al)
Na–Y	0.97	0	0	0	0	3.26
Cu–Y	0.32	0.36	0	0	0	3.29
Ni–Y	0.34	0	0.30	0	0	3.28
Co–Y	0.31	0	0	0.29	0	3.28
Ce–Y	0.35	0	0	0	0.27	3.32

even worse DMDS removal performance than the raw Na–Y zeolite, implying that Ce^{3+} has no DMDS adsorption capacity at room temperature and the exchange of Ce^{3+} leads a decrease of active sites on the surface of the raw Na–Y zeolite. From the results of these experiments, it was identified that the breakthrough adsorption capacity for DMDS was in "Cu(I)–Y > Ni–Y > Co-Y > Cu(II)–Y > Na–Y > Ce–Y" order.

3.3. Pyridine-FTIR and Raman spectra of the sorbents

In order to investigate the relationship of desulfurization performances with the type and number of surface acidic sites on the adsorbents, FT–IR spectra for the adsorption of pyridine at 200 °C and 450 °C were obtained as shown in Fig. 3. The spectrum displayed many bands in the wavenumber range of 1400–1600 cm^{-1}, which was attributed to the interaction of pyridine with Lewis (L) and Brønsted (B) acid sites on the sample surfaces. As shown in Fig. 3, the spectra presented bands of adsorption at 1450 cm^{-1} and 1550 cm^{-1}, typical of adsorbed pyridine [25]. It mainly observed the band at around 1450 cm^{-1}, arising due to ν(C–C) vibration of pyridine adsorbed at Lewis acid sites. Another band could be seen at around 1540 cm^{-1} due to the vibrations of pyridine molecules bound at bridge-bonded Brønsted acid sites. Another intense band in this spectrum at 1490 cm^{-1} arose due to contributions of both the Lewis acid and the Brønsted acid sites to pyridine adsorption [26].

Fig. 3 exhibits comparative IR spectra of different ion-exchanged zeolites, showing desorption at 200 °C after saturation adsorption of pyridine at 80 °C followed by cooling to ambient and subsequent pumping vacuum for 30 min. As shown in Fig. 3, characteristic peaks at 1540 cm^{-1} arising from the vibrations of pyridine molecules bound at the bridge-bonded Brønsted acid sites had not appeared in the spectrum E (Na–Y zeolites). In the case of Co–Y, Ni–Y and Cu(I)–Y zeolites, important changes to be noticed were a progressive increase in the intensity of the Lewis acid sites and Brønsted acid sites. Except for the difference that the peak of Ce–Y zeolite at 1450 cm^{-1} was lower than that of raw Na–Y zeolite and it had the largest Brønsted acid sites IR bands (1540 cm^{-1}). Table 3 shows that the largest proportion of the weak Lewis acid sites was observed at Cu(I)–Y zeolite, and Ce–Y zeolite has the maximum Brønsted acid sites. Furthermore, the relative intensity of above-mentioned IR bands changed considerably when the samples exposed to saturation coverage of pyridine were desorbed at 450 °C. The intensity of the bands decreased considerably with the increasing of temperature, indicating the weak bonding of pyridine at these sites. An important feature of these results is a considerable decrease in the relative intensity of Lewis acid sites compared with that shown in Fig. 3 and Table 3. Combined with desulfurization performances of the sorbents, it reveals that Lewis acid is contributed to the S–M (σ) bond between metal cation and sulfur of DMDS. In addition, Brønsted acid is harmful to the S–M (σ) bond. By the description, it is known that one of the important factors affecting adsorption desulfurization capacity is the proportion of the total weak Lewis acid sites.

Table 3
Acidic properties of different ion-exchanged zeolites ($\times 10^{-4}$ mol g^{-1}).

Catalysts	T	T_L	T_B	S_B	S_L	W_B	W_L
Na–Y	1.947	1.947	0	0	0	0	1.947
Cu(I)–Y	31.685	23.488	8.197	3.326	2.115	4.871	21.373
Ni–Y	20.503	17.464	3.039	0	1.440	3.039	16.024
Co–Y	8.228	5.416	2.812	2.564	1.041	0.248	4.375
Ce–Y	35.678	3.909	31.769	3.475	1.108	28.294	2.801

T—Total acid; T_L—total Lewis acid; T_B—total Brønsted acid; S_L—strong Lewis acid; S_B—strong Brønsted acid; W_L—weak Lewis acid; W_B—weak Brønsted acid.

Fig. 4 presents the Raman spectrum of Cu(I)–Y zeolite and the deactivation adsorbent after adsorption of DMDS. The features at 383 cm^{-1} are not observed in the spectrum of Cu(I)–Y zeolite, but are seen in the spectrum of the Cu(I)–Y zeolite after adsorption of DMDS. This region is characteristic of the Cu–S stretching vibrations [27], suggesting that DMDS should bind to the Cu^{+} with its

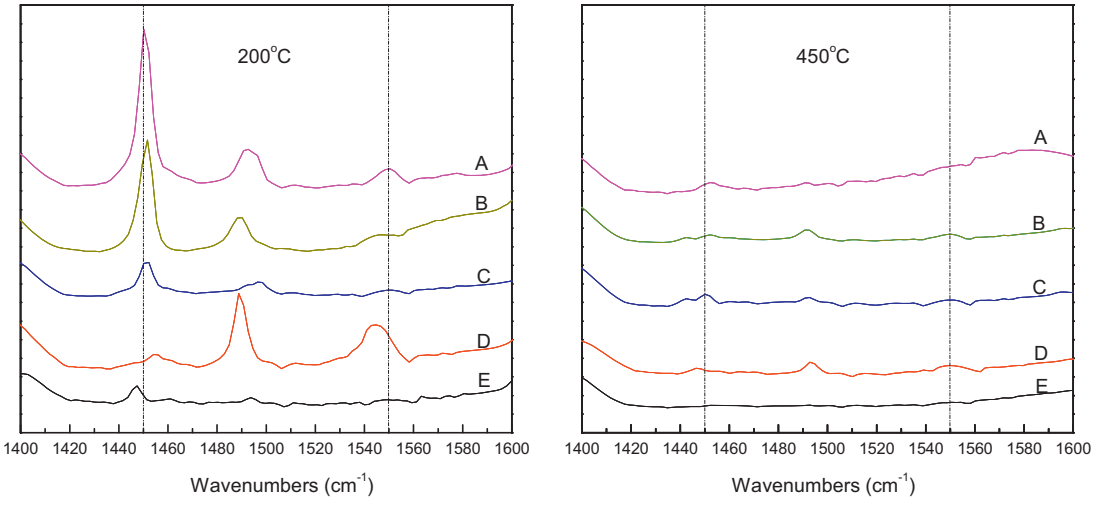

Fig. 3. Pyridine-FTIR spectra of the different ion-exchanged zeolites at 200 °C and 450 °C: (A) Cu(I)–Y (B) Ni–Y, (C) Co–Y, (D) Ce–Y, and (E) Na–Y.

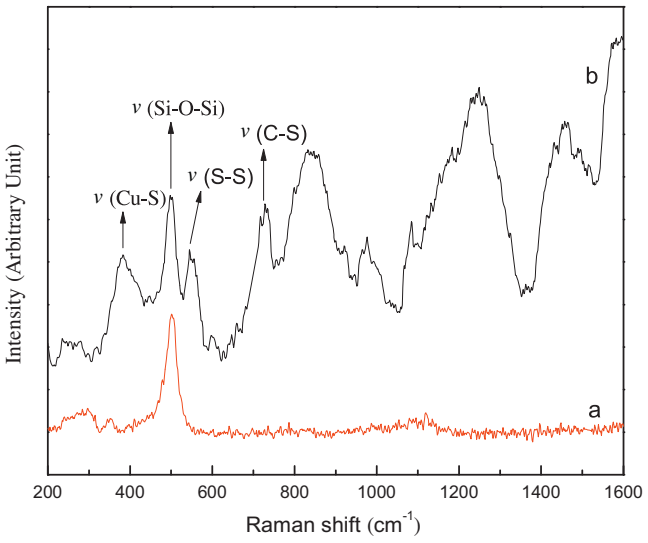

Fig. 4. The Raman spectrum of the adsorbents: (a) Cu(I)–Y zeolite, (b) after adsorption of DMDS.

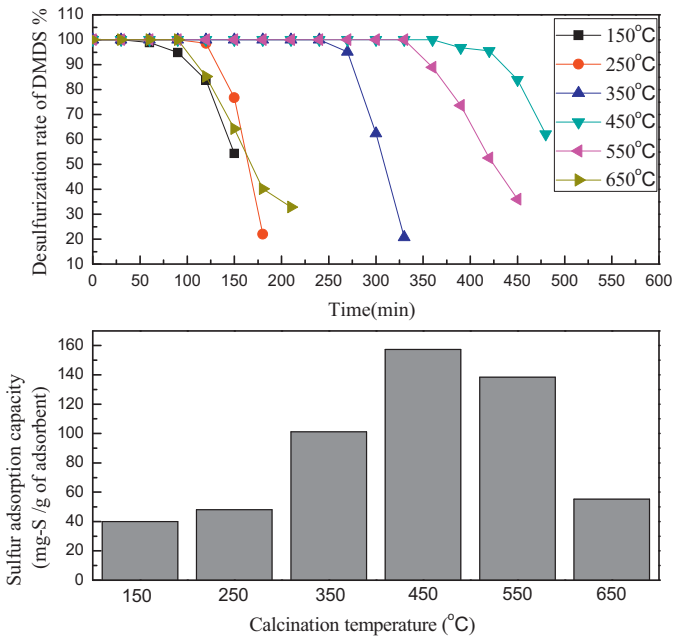

Fig. 5. Breakthrough curves and sulfur capacity for DMDS adsorption on Cu–Y zeolite following calcination at 150, 250, 350, 450, 550 and 650 °C for 5 h.

sulfur atom. The curve *b* presents bands at 725 cm^{-1}, arising from ν(C–S) vibration of DMDS adsorbed at Cu^{+} [28]. And the peak at 546 cm^{-1} in the Raman spectrum is the S–S stretching vibrations, which is characteristic of the disulphide bond. This result suggests that DMDS may adsorb on Cu^{+} without cleavage of its C–S bond and S–S band. The electronegativity of sulfur atom is not so high and it is easy to lose the lone electron pairs. Atoms of Cu^{+} ($1s^2 2s^2 2p^6 3s^2 3p^6 3d^{10} 4s^0$) can form the usual σ bonds with their empty s-orbitals, and p-orbitals. Mixing one *s* orbital and three p orbitals gives four sp^3 hybrid orbitals, which are directed toward a tetrahedral structure. The sulfur atoms of DMDS provide lone pair electrons to Cu^{+} and form the usual S–M (σ) bonds.

3.4. *Effect of calcination temperature on the performance of adsorption desulfurization.*

Different calcination temperatures ranging from 150 °C to 650 °C were tested on Cu–Y zeolites. Under the different calcination temperatures, the dynamic and static desulfurization effects of the absorbents were collected, as shown in Fig. 5. The calcination temperature has a strong influence on desulfurization performance of the modified Y zeolites. It reveals that the optimal calcination temperature of the modified Y zeolites was 450 °C and the sulfur adsorption capacity reached a maximum, was 157.4 mg S g^{-1} adsorbent.

The influence of Cu–Y zeolite calcinated at different temperature was evaluated using the differential scanning calorimetry-thermogravimetric analysis (DSC–TGA) to get more structural information. The DSC–TGA curves for our adsorbents were collected and are shown in Fig. 6. From the DTG curves of the adsorbents, the peak in the range of 20–200 °C was caused by the desorption of water adsorbed in the zeolite. As shown in Fig. 5, the sulfur removal ability of sorbent calcinated at 150 °C was lower than those calcinated at higher temperatures. Combined with DTG curves, when the calcination temperature was 150 °C, some water was absorbed in the sorbents because of the capillary force of sorbent's micropore. And the water would block the pores of the sorbents. The sorbents should be dehydrated as fully for subsequent sulfur adsorption. From the DTG curves of Cu(II)–Y zeolite, peak at

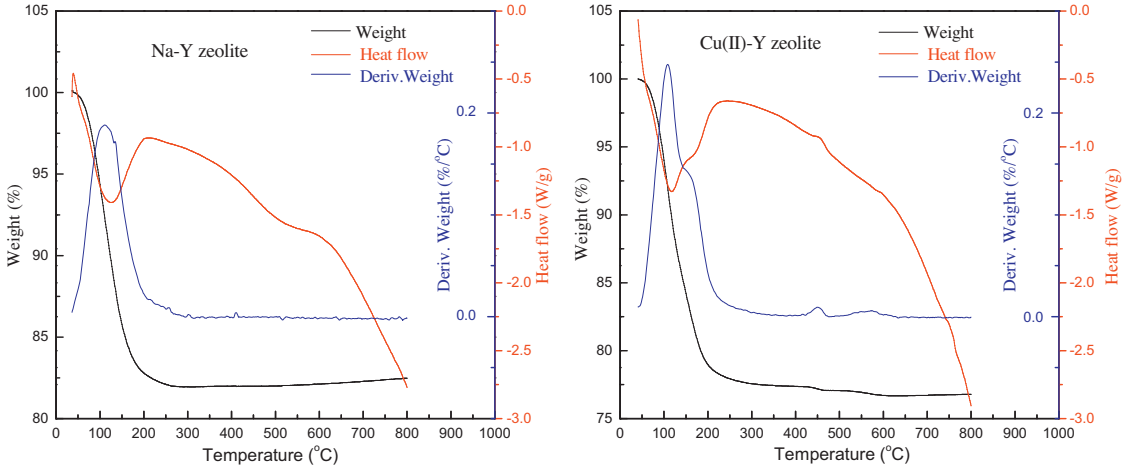

Fig. 6. DSC–TGA curves in nitrogen for the Na-Y zeolite and Cu(II)-Y zeolite.

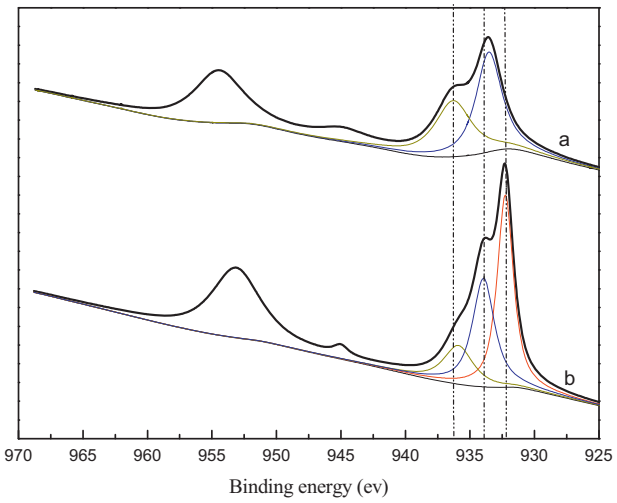

Fig. 7. X-ray Photoelectron Spectroscopy (XPS) patterns of copper ion on Cu-Y zeolites calcinated at different temperatures: (a) calcinated at 150 °C, (b) calcinated at 450 °C.

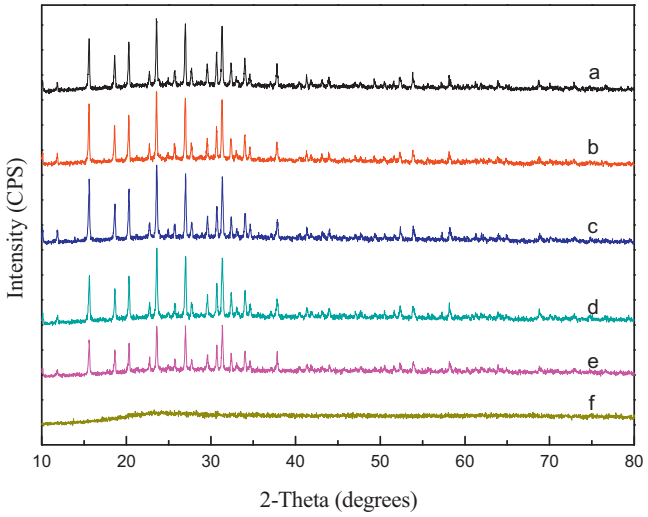

Fig. 8. X-ray diffraction patterns on Cu–Y zeolites with different calcination temperatures: (a) 250 °C, (b) 350 °C, (c) 450 °C, (d) 550 °C, (e) 650 °C and (f) 800 °C.

about 450 °C can be observed, but are not appeared in the curves of the NaY zeolite. This differences may be caused by the autoreduction of cupric ions to cuprous ions in an inert atmosphere at high temperatures. It indicated that Cu(II)–Y zeolite may transform into Cu(I)–Y zeolite which had a better desulfurization performance.

The XPS analysis on copper ions on the adsorbent was carried out to demonstrate this phenomenon, and the results are presented in Fig. 7. The characteristics of divalent copper, Cu^{2+} can be confirmed by the Cu $2p_{3/2}$ binding energy within the range of 933–936 eV and the shake-up satellite peak. Monovalent copper can be assigned to the binding energy of the XPS peaks ranging from 932 to 933 eV without any shake-up satellite peaks. Contarini et al. [29] interpreted the behavior of the Cu $2p_{3/2}$ photoelectron lines in Cu–Y zeolite in terms of coordination state changes of the metal ion. The characteristics of divalent copper with shake-up satellite peak, at higher binding energy (~ 935–936 eV) is assigned to octahedrally coordinated Cu^{2+}, while the component at lower binding energy (~ 933–934 eV) is assigned to tetrahedrally coordinated Cu^{2+}. As shown in the Fig. 7, the copper in the Cu–Y zeolite calcinated at 150 °C existed in a form of Cu^{2+} and two peaks at 933.8 and 936.2 eV binding energy were assigned to tetrahedral and octahedral Cu^{2+} species, respectively. The characteristic peak of the Cu $2p_{3/2}$ arising at 932.2 eV can be seen in the XPS patterns of Cu–Y zeolite calcinated at 450 °C. Although the autoreduction of cupric ions to cuprous ions had occurred in an inert atmosphere at high temperatures, the presence of Cu^{2+} had also been observed on the surface of the adsorbent. Because the Cu^{2+} cannot absolutely change into Cu^{+} in the inert atmosphere. The XPS spectra of the adsorbents contain a Cu $2p_{3/2}$ shake-up satellite peak at 944.8 eV and their intensities decrease as the calcination temperature increasing.

The modified Y zeolites baked at different calcination temperature were further characterized by X-ray diffraction (XRD) to get more structural information, as shown in Fig. 8. When the calcination temperature was under 650 °C, the crystal structure of Cu–Y was still stable. However, the crystallinities of the adsorbents decreased at high calcination temperature and characteristic diffraction peaks of zeolite all disappeared when the calcination temperature was 800 °C. That may be caused by the collapse of crystal structure and exist in the amorphous structure. Integrated the analysis of DSC–TGA, XPS and XRD, the desulfurization performance on Cu–Y zeolite was caused by both valence state of copper ions and crystallinities of the adsorbent.

3.5. *Effect of reaction temperature on adsorption of DMDS.*

In order to study the effect of activation temperature, different reaction temperatures were tested on Cu(I)–Y zeolite calcinated at 450 °C. The desulfurization test results presented in Fig. 9 revealed that the reaction activity decreased with an increasing of reaction temperature. It is well known that the temperature increment could accelerate the response rate but complexation adsorption reaction is an exothermic reaction. So the temperature increment might adverse to the adsorption reaction. The low temperature was in favour of the adsorption reaction.

3.6. *TPD of DMDS analysis*

TPD technique is a useful technique of surface analysis. It is usually used to estimate binding energy of adsobates and activated energy of desorption, which can be used to value the adsorbents and estimate adsorption isotherms [30]. The kinetics of the

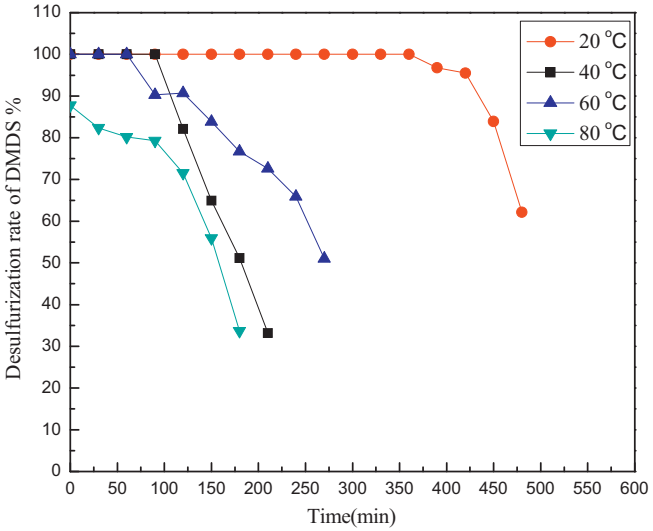

Fig. 9. Effect of reaction temperature on adsorption performance of the Cu(I)–Y zeolite calcinated at 450 °C.

Table 4
Desorption peak temperatures of DMDS at different heating rates and activation energies of desorption on various zeolites.

Adsorbents	T_P (K) corresponding to peaks of TPD curves at different heating rate β_H (K min^{-1})				Activation energy of desorption (E_A, kJ mol^{-1})
	5	8	10	12	
Na–Y zeolite	475.2	497.6	509.8	528.3	24.2
Cu(I)–Y zeolite	488.2	496.0	505.3	513.8	60.4

desorption process can be assumed by Polanyi–Wigner formula [31],

$$\gamma_d = -\frac{d\theta_A}{dt} = k_0\theta_A^n \exp\left(\frac{E_A}{RT}\right) \quad (4)$$

Here the desorption of DMDS from modified zeolites is assumed to follow first order kinetics, and then the activated energy of desorption can be formulated.

$$\ln\left(\frac{RT_P^2}{\beta_H}\right) = \frac{E_A}{R}\left(\frac{1}{T_P}\right) + \ln\left(\frac{E_A}{k_0}\right) \quad (5)$$

where γ_d is the rate of desorption, TP is the temperature of desorption peak, EA is activated energy of desorption, R is a gas constant, β_H is the heating rate, k_0 is the preexponential of the rate constant for desorption. Therefore, a plot of $\ln\left(RT_P^2/\beta_H\right)$ versus $1/T_P$ will yield a line with slop E_A/R and the activated energy of desorption (E_A) could be obtained.

Fig. 10 show the TPD spectrum of DMDS on the raw Na–Y and Cu(I)–Y zeolite at the different heating rate of 5–12 K min^{-1}, respectively. As shown in Fig. 10, the desorption peak temperatures (T_P) of Na–Y zeolite can be observed at 475.2, 497.6, 509.8 and 528.3 K at the heating rate of 5, 8, 10 and 12 K min^{-1}, respectively. On the TPD–DMDS on Cu(I)–Y zeolite, two peaks are observed which represent different kinetic process. Mashkina et al. [32] reported that DMDS could decompose into dimethyl sulfide, methyl mercaptan and hydrogen sulfide with existence of Lewis acid on the zeolite surfaces. The first peak was the desorption of DMDS on Cu(I)–Y zeolite and the other one was caused by the decomposition of DMDS. The desorbed adsorbates of the second peak were measured by the gas chromatography and mass spectrometer (GC–MS) and the main decomposition product was methyl mercaptan. As shown in Fig. 10, the intensity of the desorption peak of DMDS on Cu(I)–Y zeolite appeared to be larger than those on the Na–Y zeolite. It also confirmed the DMDS removal capacity of adsorbent was improved after ion exchange of copper ions.

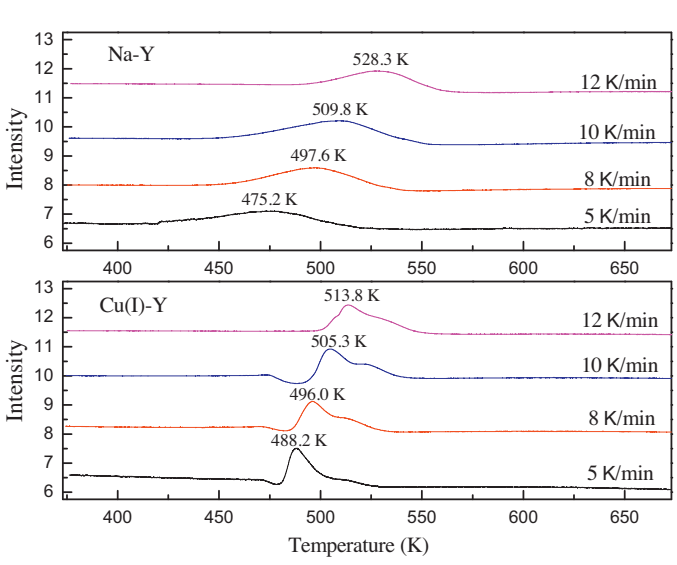

Fig. 10. DMDS–TPD patterns for Na–Y and Cu(I)–Y zeolites at the different heating rate.

Table 4 shows the desorption peak temperatures, T_P, corresponding to the desorption peaks of TPD curves of DMDS on the zeolites at different heating rates. The T_P increased with the increasing of heating rate. Knowing a series of T_P at different heating rate, one can estimate desorption activated energy of DMDS on the zeolites by using Eq. (2). The calculation results of desorption activated energy of DMDS on the zeolites were also listed in Table 4. The desorption activated energy of DMDS on the Cu(I)–Y zeolite, E_A = 60.4 kJ mol^{-1}, was higher than that of DMDS on the Na–Y zeolite. The higher desorption activated energy, the more difficult desorption of the adsorbate from an adsorbent. The transition metal ions Cu^+ is complexible, and so the S–M (σ) bond between DMDS and metal ions may be formed to increase adsorption bond energy of DMDS on the adsorbents.

3.7. Regeneration performance

Desulfurization adsorbents are required to be regenerable for multiple cycles to reduce the operational cost and adsorbent material cost. Regeneration tests of Cu(I)–Y zeolite were carried out in the fixed bed after adsorption of DMDS. Nitrogen or air was added to the reactor at the rate of 50 mL per minute, while the temperature was raised from room temperature to 450 °C at the rate of 10 °C min^{-1} and maintained for 4 h at 450 °C. Effects of the regeneration in different ambient atmospheres and regeneration circulating times are shown in Fig. 11. Compared with the fresh Cu(I)–Y zeolite, the adsorption desulfurization property of deactivation adsorbent can be partial recovered after regeneration in air or N_2 atmosphere at 450 °C for 4 h. However, the regeneration process of deactivation adsorbent was carried out in air at 450 °C for 4 h and then switched into N_2 atmosphere for 4 h at the same temperature. And the desulfurization performance of the adsorbent can be recovered obviously. After three times of cyclic regeneration, desulfurization property of the adsorbent can still be recovered to 66.7%. The DMDS absorbed on adsorbent can be fully burned at 450 °C in air, nevertheless, cuprous ions were oxidated to cupric ions. After that the recurrence of autoreduction could conducted in N_2 atmosphere at high temperatures. Only in the N_2 regeneration, sulfur on the adsorbent may not be removed completely and the regeneration effect was unsatisfactory.

The Pyridine-FTIR spectra of the regenerated Cu(I)–Y zeolites were carried out to evaluate the surface acidic sites on the adsorbents after regeneration. As shown in Fig. 12, characteristic peaks at 1450 cm^{-1} arising from the ν(C–C) vibration of pyridine adsorbed at Lewis acid sites could then weaken as the increase of regeneration times. Table 5 shows that the largest proportion of the weak Lewis acid sites was observed at the fresh Cu(I–Y zeolite. It reveals that

Table 5
Acidic properties of regenerated Cu(I)–Y zeolites ($\times 10^{-4}$ mol g^{-1}).

Catalysts	T	T_L	T_B	S_B	S_L	W_B	W_L
Fresh	31.685	23.488	8.197	3.326	2.115	4.871	21.373
First time	23.641	15.671	7.970	0	1.369	7.970	14.302
Second time	15.969	12.613	3.356	0	0.847	3.356	11.766
Third time	10.549	7.382	3.212	0	0.683	3.212	6.699

T—Total acid; T_L—total Lewis acid; T_B—total Brønsted acid; S_L—strong Lewis acid; S_B—strong Brønsted acid; W_L—weak Lewis acid; W_B—weak Brønsted acid.

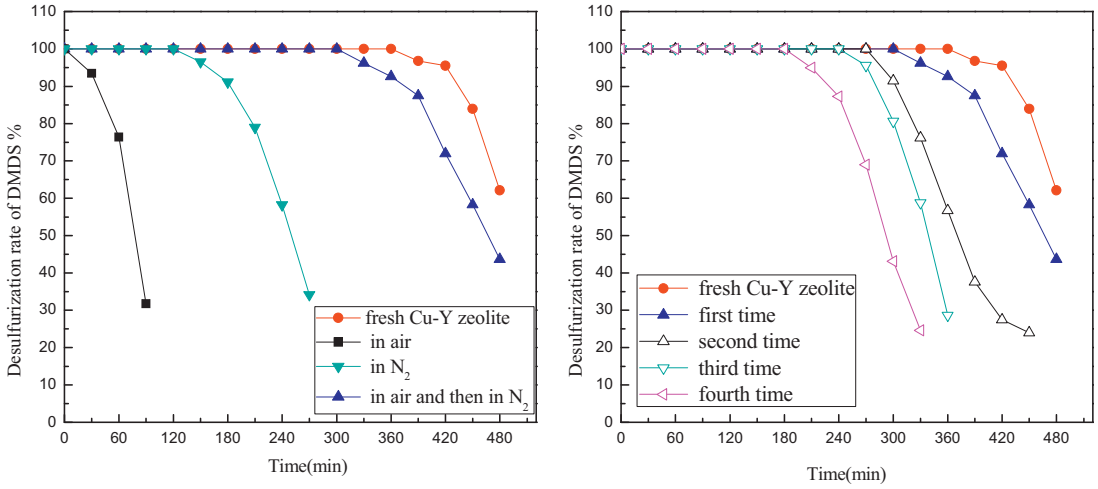

Fig. 11. Breakthrough curves for DMDS adsorption on adsorbents after regeneration in different atmosphere at 450 °C and regeneration time in air and then in N_2 at 450 °C.

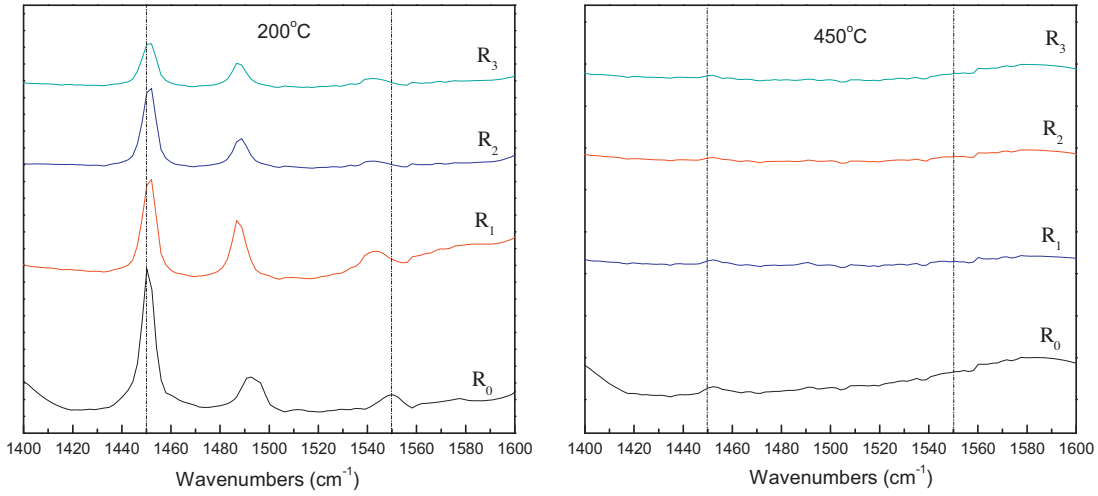

Fig. 12. Pyridine-FTIR spectra of the regenerated Cu(I)–Y zeolites at 200 °C and 450 °C: (R_0) fresh Cu(I)–Y zeolite, (R_1) first time regeneration, (R_2) second time regeneration, and (R_3) third time regeneration.

the regeneration process can cause the decrease of Lewis acid sites on the adsorbents. Combined with desulfurization performances of the regenerated sorbents, it also reveals that Lewis acid is contributed to the S–M (σ) bond between metal cation and sulfur of DMDS. The deactivation adsorbents after regeneration were further characterized by XRD, as shown in Fig. 13. With the increasing of regeneration times, the characteristic diffraction peaks and crystallinities of the adsorbents decreased which may be caused by the collapse of crystal structure. Through the analysis of Pyridine-FTIR spectra and XRD, the Lewis acid sites and crystal structure can be destroyed in the regeneration process and then affect the desulfurization performance of DMDS on Cu(I)–Y zeolite.

3.8. In situ FTIR of the adsorption and thermal desorption of sulfur on adsorbent

Fig. 14 displays the in situ FTIR spectra recorded from the adsorption and thermal desorption of DMDS on Na–Y zeolite. The left and right panels show the ν_{C-H} region and low wavenumber region, respectively. Several bands located at 2994, 2921, and 2818 cm^{-1} were observed in the 3000∼2800 cm^{-1} range which are attributed to aliphatic ν_{C-H} modes [33]. Before the adsorption of DMDS, absorbance features at the range of 3000–2800 cm^{-1} can not be seen in the spectra of raw Na–Y zeolite (Fig. 14, right

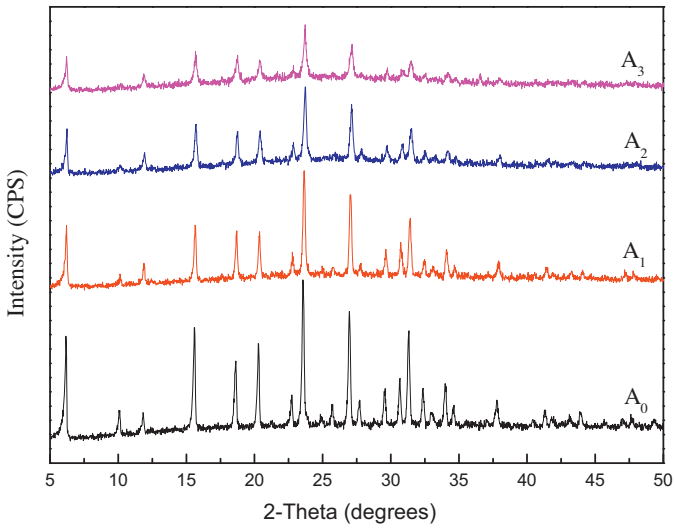

Fig. 13. X-ray diffraction patterns on regenerated Cu(I)–Y zeolites: (A_0) fresh Cu(I)–Y zeolite, (A_1) first time regeneration, (A_2) second time regeneration, and (A_3) third time regeneration.

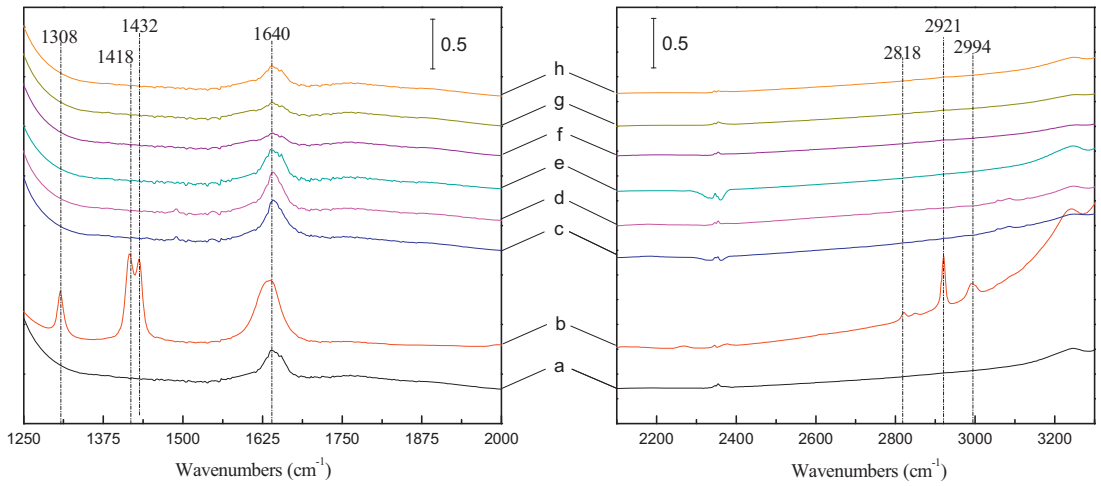

Fig. 14. In situ FTIR spectra recorded from the adsorption and thermal desorption of DMDS on Na–Y zeolite; (a) after pretreatment, (b) adsorption of DMDS at ambient temperature, (c) desorption at 50 °C, (d) desorption at 100 °C, (e) desorption at 150 °C, (f) desorption at 200 °C, (g) desorption at 250 °C, and (h) desorption at 300 °C.

a). This indicates that peaks at 2994 [$\nu_{as}(CH_3)$], 2921 [$\nu_{as}(CH_3)$], and 2818 cm^{-1} [$\nu_s(CH_3)$] are attributed to the methyl group of DMDS absorbed on the zeolite via physical intermolecular force and other interactions. And the intensity of the bands decreased sharply with increasing temperature and disappeared when the temperature up to 50 °C. It indicated the interaction between DMDS and Na–Y zeolite is weak and the DMDS adsorbed on Na–Y zeolite can be easily desorbed with increasing temperature under the vacuum condition. In the low wavenumber region, additional spectral features compared with raw Na–Y zeolite are located at 1432, 1418 and 1308 cm^{-1}, which are attributed to $\delta_{as}(CH_3)$ and $\delta_s(CH_3)$ of the CH_3–S–S–CH_3. The absorbance bands at 1432 and 1418 cm^{-1} can be reasonably assigned to DMDS coordinated via its sulfur atom to coordinative unsaturated (cus) metal sites and Si–OH sites on the Na–Y zeolite support, respectively [34]. However, the intensity of the bands diminished rapidly with increasing temperature, and nearly vanished when the temperature increased to 50 °C. And the bands at 1640 cm^{-1} can be assigned to the hydroxide radical vibrations of water adsorbed in the zeolite.

Fig. 15 shows the in situ FTIR spectra recorded from the adsorption and thermal desorption of DMDS on the Cu(I)–Y zeolite. The left and right panels show the $\nu_{C\text{-}H}$ region and low wavenumber region, respectively. Three bands located at 2997, 2921, and 2818 cm^{-1} were found after the adsorption of DMDS in the 3000–2800 cm^{-1} range attributed to $\nu_{C\text{-}H}$ modes of adsorbed DMDS via physical intermolecular force and other interactions. The bands remained until the desorption temperature increased to 150 °C under the vacuum condition, indicating that the interaction between DMDS and adsorbent was strengthened by introducing copper species to the zeolite. In the low wavenumber region, the additional spectral features are located at 1424, 1416, and 1306 cm^{-1}, which are attributed to $\delta_{as}(CH_3)$ and $\delta_s(CH_3)$ of the CH_3–S–S–CH_3. The intensity of bands at 1424 cm^{-1} after the adsorption of DMDS on modified Y zeolite through its sulfur atom to coordinative unsaturated (cus) copper sites (S–M (σ) bond) was stronger than the one on raw Na–Y zeolite and the band was still existed until the desorption temperature rose to 150 °C. It can be concluded that the amounts of DMDS molecules adsorbed on modified Y zeolite via S–M (σ) bond are much more than on raw Na–Y zeolite and the

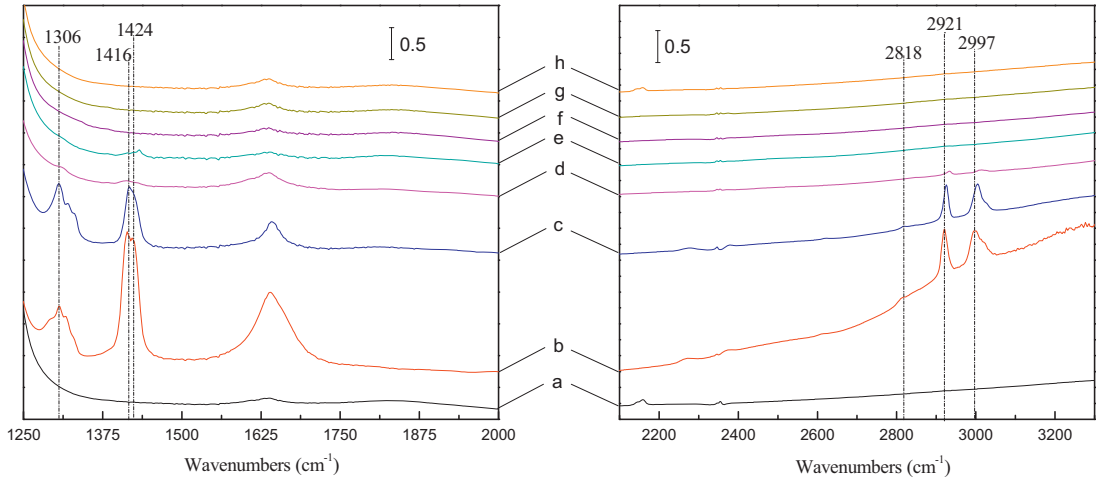

Fig. 15. In situ FTIR spectra recorded from the adsorption and thermal desorption of DMDS on Cu(I)–Y zeolite; (a) after pretreatment, (b) adsorption of DMDS at ambient temperature, (c) desorption at 50 °C, (d) desorption at 100 °C, (e) desorption at 150 °C, (f) desorption at 200 °C, (g) desorption at 250 °C, and (h) desorption at 300 °C.

interaction of DMDS molecules with cuprous ions is stronger than with raw Na–Y zeolite.

The combined techniques of Raman spectrum, DMDS–TPD and in situ FTIR spectroscopy have been used to investigate the adsorption and desorption behavior of DMDS on modified Y zeolites. Two interaction patterns were found between DMDS and zeolites: the first pattern is DMDS adsorbed on raw Na–Y zeolite via physical intermolecular force, and the other one is DMDS coordinated via its sulfur atom to unsaturated (cus) metal sites (S–M (σ) bond) on the ion-exchanged zeolites. The formation of S–M (σ) bond between DMDS and metal ions could increase adsorption bond energy (E_A) of DMDS on the adsorbents. Thermal desorption of DMDS absorbed on Cu(I)–Y zeolite was carried through two different kinetic processes: the one desorption process is the breakage of S–M (σ) bond between DMDS and cuprous ions, the other one is the decomposition of DMDS into dimethyl sulfide, methyl mercaptan and hydrogen sulfide with existence of Lewis acid on the zeolite surfaces at a higher temperature.

4. Conclusions

Several transition metals were used to modify the Na–Y zeolite and Cu(I)–Y zeolite exhibited the best DMDS removal performance from liquid hydrocarbon streams. The Cu(I)–Y zeolite calcinated at 450 °C in the inert atmosphere exhibited a optimal saturated sulfur capacity of 157.4 mg S g^{-1} adsorbent. Pyridine-FTIR analyses indicated that the weak Lewis acid sites contributed to the adsorption of sulfur compounds and the Brønsted acid is harmful to the S–M (σ) bond. The characteristic of the Cu–S, C–S and S–S stretching vibrations were found in the Raman spectrum of the Cu(I)–Y zeolite after the adsorption of DMDS. Integrated the analysis of DSC–TGA, XPS and XRD, the desulfurization performance on Cu–Y zeolite was caused by both valence state of copper ions and crystallinities of the adsorbent. The best regeneration performance was obtained through the process of air and N_2 treatment at 450 °C. The results of combined techniques of DMDS–TPD and in situ FTIR spectroscopy revealed that adsorption of DMDS on modified Y zeolites occurred via multilayer intermolecular forces and S–M (σ) bonds. And the S–M (σ) bond between DMDS and copper ions were formed to increase adsorption bond energy of DMDS on the adsorbents.

Acknowledgments

This work is financially supported byNational Natural Science Foundation of China(no.21276086) andOpening Project of State Key Laboratory of Chemical Engineering of East China University of Science and Technology(no.SKL-ChE-11C04).

References

[1] B. Calderon, I. Aracil, A. Fullana, Chemical Engineering Journal 183 (2012) 325–331.
[2] J. Lee, H.T. Beum, C.H. Ko, S.Y. Park, J.H. Park, J.N. Kim, B.H. Chun, S.H. Kim, Industrial & Engineering Chemistry Research 50 (2011) 6382–6390.
[3] A.J. Hernández-Maldonado, R.T. Yang, AIChE Journal 50 (2004) 791–801.
[4] B. Guo, R. Wang, Y. Li, Fuel Processing Technology 91 (2010) 1731–1735.
[5] D. Li, Chinese Journal of Catalysis 34 (2013) 48–60.
[6] A.J. Hernández-Maldonado, R.T. Yang, Catalysis Reviews 46 (2004) 111–150.
[7] R.T. Yang, A.J. Hernández-Maldonado, F.H. Yang, Science 301 (2003) 79–81.
[8] A.J. Hernández-Maldonado, R.T. Yang, Journal of the American Chemical Society 126 (2004) 992–993.
[9] A.J. Hernández-Maldonado, R.T. Yang, Industrial & Engineering Chemistry Research 42 (2003) 3103–3110.
[10] A.J. Hernández-Maldonado, F.H. Yang, G. Qi, R.T. Yang, Applied Catalysis B: Environmental 56 (2005) 111–126.
[11] A. Takahashi, F.H. Yang, R.T. Yang, Industrial & Engineering Chemistry Research 41 (2002) 2487–2496.
[12] W. Wardencki, R. Staszewski, Journal of Chromatography A 91 (1974) 715–722.
[13] S. Mikhail, T. Zaki, L. Khalil, Applied Catalysis A: General 227 (2002) 265–278.
[14] X. Meng, H. Huang, H.X. Weng, L. Shi, Bulletin of Korean Chemical Society 33 (2012) 3213–3217.
[15] M. Xuan, H.X. Weng, L. Shi, China Petroleum Processing and Petrochemical Technology 14 (2012) 25–30.
[16] X.L. Tang, W. Qian, A. Hu, Y.M. Zhao, N.N. Fei, L. Shi, Industrial & Engineering Chemistry Research 50 (2011) 9363–9367.
[17] M. Seredych, T.J. Bandosz, Fuel Processing Technology 91 (2010) 693–701.
[18] Y.A. Alhamed, H.S. Bamufleh, Fuel 88 (2009) 87–94.
[19] X.L. Ma, S. Velu, J.H. Kim, C.S. Song, Applied Catalysis B: Environmental 56 (2005) 137–147.
[20] A. Ryzhikov, I. Bezverkhyy, J.P. Bellat, Applied Catalysis B: Environmental 84 (2008) 766–772.
[21] C.S. Shalaby, S.K. Saha, X.L. Ma, C.S. Song, Applied Catalysis B: Environmental 101 (2011) 718–726.
[22] S.C. Larsen, A. Aylor, A.T. Bell, J.A. Reimer, Journal of Chemical Physics 98 (1994) 11533–11540.
[23] D.J. Parrillo, D. Dolenec, R.J. Gorte, R.W. Mccabe, Journal of Catalysis 142 (1993) 708–718.
[24] A.J. Hernaíndez-Maldonado, R.T. Yang, Industrial & Engineering Chemistry Research 42 (2003) 123–129.
[25] H. Vinh-Thang, Q.L. Huang, A. Ungureanu, M. Eić, D. Trong-On, S. Kaliaguine, Microporous and Mesoporous Materials 92 (2006) 117–128.
[26] P. Kalita, N.M. Gupta, R. Kumar, Journal of Catalysis 245 (2007) 338–347.
[27] C.R. Andrew, H. Yeom, J.S. Valentine, B.G. Karlsson, N. Bonander, G. Pouderoyen, G.W. Canters, T.M. Loehr, J.S. Loeh, Journal of the American Chemical Society 116 (1994) 11489–11498.
[28] S. Cho, E.S. Park, K. Kim, M.S. Kim, Journal of Molecular Structure 479 (1999) 83–92.
[29] S. Contarini, L. Kevan, Journal of Chemical Physics 90 (1986) 1630–1632.
[30] H.X. Xi, Z. Li, H.B. Zhang, X. Li, X.J. Hu, Separation and Purification Technology 31 (2003) 41–45.
[31] R.J. Cvetanovic, Y. Amenomiya, Catalysis Reviews 6 (1972) 21–46.
[32] A.V. Mashkina, E.A. Paukshtis, O.P. Krivoruchko, L.N. Khairulina, Kinetics and Catalysis 49 (2008) 266–273.
[33] H. Huang, D.Z. Yi, Y.N. Lu, X.L. Wu, Y.P. Bai, X.M.L. Shi, Chemical Engineering Journal 225 (2013) 447–455.
[34] S.T. Oyama, T. Gott, K. Asakura, S. Takakusagi, K. Miyazaki, Y. Koike, K.K. Bando, Journal of Catalysis 268 (2009) 209–222.